



## Article

# Parameter Extraction of Accelerated Moving Targets under Non-quasi-axial Incidence Conditions Based on Vortex Electromagnetic Wave Radar

Lingling Zhang <sup>1</sup> , Yongzhong Zhu <sup>1,\*</sup>, Yijun Chen <sup>1,2</sup>, Wenxuan Xie <sup>1</sup> and Hang Yuan <sup>3</sup>

<sup>1</sup> College of Information Engineering, Engineering University of the PAP, Xi'an 710086, China; zhanglingling528@163.com (L.Z.); chenijun519@126.com (Y.C.); bsbs1980@sina.com (W.X.)

<sup>2</sup> The National Key Laboratory of Radar Signal Processing, Xidian University, Xi'an 710071, China

<sup>3</sup> The Institute of Information and Navigation, Air Force Engineering University, Xi'an 710077, China; yuanhang517300@163.com

\* Correspondence: haiyihaiyi@hotmail.com

**Abstract:** Vortex electromagnetic wave radar carrying orbital angular momentum can compensate for the deficiency of planar electromagnetic wave radar in detecting motion parameters perpendicular to the direction of electromagnetic wave propagation, thus providing more information for target recognition, which has become a hot research field in recent years. However, existing research makes it difficult to obtain the acceleration and rotation centers of targets under non-quasi-axial incidence conditions of vortex electromagnetic waves. Based on this, this article proposes a variable speed motion target parameter extraction method that combines single element and total element echoes. This method can achieve three-dimensional information extraction of radar targets based on a uniform circular array (UCA). Firstly, we establish a non-quasi-axis detection echo model for variable-speed moving targets and extract echoes from different array elements. Then, a single element echo is used to extract the target's range slow time profile and obtain the target's rotation center  $z$  coordinate. We further utilize the target linear, angular Doppler frequency shift extremum, and median information to extract parameters such as target acceleration, tilt angle, rotation radius, and rotation center  $x$  and  $y$  coordinates. We analyzed the impact of different signal-to-noise ratios and motion states on parameter extraction. The simulation results have verified the effectiveness of the proposed algorithm.

**Keywords:** vortex electromagnetic wave; non-quasi-axis incidence; variable speed motion; parameter extraction



**Citation:** Zhang, L.; Zhu, Y.; Chen, Y.; Xie, W.; Yuan, H. Parameter Extraction of Accelerated Moving Targets under Non-quasi-axial Incidence Conditions Based on Vortex Electromagnetic Wave Radar. *Remote Sens.* **2024**, *16*, 1931. <https://doi.org/10.3390/rs16111931>

Academic Editors: Yin Zhang, Deqing Mao, Yulin Huang and Yachao Li

Received: 13 April 2024

Revised: 18 May 2024

Accepted: 24 May 2024

Published: 27 May 2024



**Copyright:** © 2024 by the authors. Licensee MDPI, Basel, Switzerland. This article is an open access article distributed under the terms and conditions of the Creative Commons Attribution (CC BY) license (<https://creativecommons.org/licenses/by/4.0/>).

## 1. Introduction

Traditional radar detection systems [1–4] mainly rely on the relative motion of the radar and the target along the line of sight direction, that is, a linear Doppler frequency shift, to obtain the motion information of the target. However, because of how planar electromagnetic waves work, the line Doppler frequency shift of the target echo will disappear when the target's motion is perpendicular to the direction of its propagation. This means that the target cannot be recognized. Unlike planar electromagnetic waves, vortex electromagnetic waves carrying orbital angular momentum have a spiral-phase wavefront, which can provide a new dimension of information [5] for target detection. By utilizing its unique rotational Doppler frequency shift, it is possible to simultaneously observe information perpendicular to and parallel to the direction of the electromagnetic wave propagation. Therefore, in recent years, it has been applied in more and more fields [6–14], such as wireless communication, quantum manipulation, radar imaging, rotational Doppler frequency shift detection, etc.

In the specific application of vortex electromagnetic wave detection, some scholars have studied the parameter extraction of variable-speed motion targets under quasi-axial

incidence conditions. Reference [15] proposed an algorithm for extracting the acceleration of uniformly accelerating rotating targets using methods such as the Wigner Ville distribution and fractional Fourier transform, with a focus on analyzing the impact of the spectral width of the time–frequency spectrum on the acceleration resolution. Furthermore, reference [16] proposed a decoupling and detection method combining multimodal and Choi Williams distribution (CWD), which achieved the simultaneous extraction of the translational and rotational acceleration of composite moving targets. The influence of different modal combinations and vortex electromagnetic wave purities on parameter extraction accuracy was analyzed. Subsequently, reference [17] achieved the extraction of acceleration for variable acceleration moving targets under multiple scattering point conditions based on the non-differentiable point features in the echo, as well as the minimum sum of the mean square error and the expected error between the real signal and the estimated signal. At the same time, the algorithm also improved the minimum resolution of acceleration detection for composite moving targets.

However, in practical detection, for non-cooperative targets, quasi-axial incidence is clearly difficult to achieve. A large number of scholars have conducted research on this issue in non-quasi-axis detection scenarios. Due to the fact that the echo signals of rotating objects are often non-linear, non-stationary, and time-varying, classic methods such as time–frequency analysis are often used to transform edge detection problems into peak detection problems in parameter space to extract the micro-motion features of targets. Reference [18] analyzed and derived the Doppler frequency shift and micro-Doppler frequency shift formulas for targets at any position, and they proposed two-parameter extraction algorithms under special non-quasi-axis conditions based on time–frequency analysis: in their work, the rotation center was located on the Z axis, and the rotation plane was parallel to the radar reference coordinate system on the XOY plane, but the estimation accuracy was limited by the resolution of the time–frequency analysis. Furthermore, reference [19] achieved the extraction of the rotation radius and tilt angle of a single scattering point target at any position based on the Hough transform. Subsequently, reference [20] focused on analyzing the relationship between the maximum and minimum time intervals of angular Doppler frequency and micro-motion parameters. Based on the known rotation center, the iterative soft threshold algorithm was used to obtain the fine micro-motion parameters of multiple scattering points. Subsequently, reference [21] proposed a two-step estimation algorithm for micro-motion parameters. Based on a smooth pseudo Wigner Ville distribution spectrum and particle swarm optimization algorithm, the extraction of parameters such as the angular frequency, ratio of deflection distance to rotation radius, and rotation attitude under unknown rotation center conditions was achieved, and the Cramér–Rao bound for micro-motion parameter estimation was derived. In addition, networked radar is also a classic method for extracting target micro-motion parameters. Reference [22] proposed a method for jointly extracting target precession and size features based on the instantaneous frequency variation relationship of target scattering points under different radar perspectives using narrowband radar networking. This method achieved high-precision estimation of parameters such as cone target height, base radius, center of mass position, and precession angle. In the application of vortex electromagnetic waves, reference [23] proposed a parameter extraction method based on a combination of vortex and broadband electromagnetic wave radars, which combined a micro-Doppler frequency shift and high-resolution range profile. This method achieved the extraction of the precession and structural parameters of ballistic targets moving parallel to the ground. However, the above studies are all based on the uniform motion of the target, and it is not yet possible to extract the micro-motion parameters of the variable speed moving target. The extracted parameters mainly focus on the characteristics of the target's rotation speed, rotation radius, initial phase, etc. Further research is needed on how to simultaneously extract the target's motion, structure, position, and other parameters under the conditions of unknown target rotation center and low system complexity.

In order to solve the above problems, this article proposes a variable-speed motion target parameter extraction algorithm based on the non-quasi-axis incidence condition of vortex electromagnetic wave radar and successfully extracts the target's tilt angle, rotation radius, rotation speed, acceleration, variable acceleration quadratic coefficient, rotation center, and rotation initial phase. Firstly, based on the acceleration motion model under non-quasi-axis incident conditions, the target echo equation is established, and the echo signal of a single antenna element is extracted to obtain the radial distance slow time variation of the target. Based on this, the  $z_o$  coordinate of the target rotation center is extracted. Secondly, the formation mechanism of extreme values and median values in the line Doppler frequency shift curve of the total echo of the target is analyzed, and formulas for solving parameters such as acceleration and initial phase are derived. Then, we combine the extracted parameters and the trust domain dogleg algorithm [24] to solve the non-linear system of equations. We analyze the impact of different motion states and signal-to-noise ratio (SNR) conditions on the accuracy of parameter extraction. Finally, the simulation results verify the effectiveness of the proposed algorithm.

The chapter arrangement of this article is as follows: Section 2 establishes an echo model for variable-speed moving targets in non-quasi-axis detection scenarios. Section 3 studies the relationship between the median and extreme values in the frequency shift curve and the target acceleration and proposes methods for separating and extracting different parameters. Section 4 simulates the algorithm proposed in this article and analyzes the effectiveness and robustness of the method under different motion parameters and signal-to-noise ratio conditions. Finally, the conclusion is presented in Section 5.

## 2. Echo Model of Variable-Speed Moving Targets under Non-Quasi-Axis Detection Conditions

As shown in Figure 1, a single transmitter multiple receiver uniform circular array (UCA) device is used to generate vortex electromagnetic waves, and the geometric relationship between the radar and the target is shown in the figure. Let  $O - XYZ$  be the radar coordinate system, let  $o - xyz$  be the reference coordinate system, and let  $o - x'y'z'$  be the local coordinate system of the target. If the target undergoes variable-speed motion around the  $z'$  axis at a rotational speed of  $\Omega(t)$  in the  $x'o'y'$  plane, with a rotation radius of  $r$ , its coordinates in the radar coordinate system can be obtained as

$$\begin{bmatrix} X_Q(t) \\ Y_Q(t) \\ Z_Q(t) \end{bmatrix} = \mathbf{R}_{\text{init}} \cdot \begin{bmatrix} r \cos(2\pi(\Omega_0 t + \frac{1}{2}g_A t^2 + \frac{1}{6}b_A t^3) + \phi) \\ r \sin(2\pi(\Omega_0 t + \frac{1}{2}g_A t^2 + \frac{1}{6}b_A t^3) + \phi) \\ 0 \end{bmatrix} + \begin{bmatrix} x_o \\ y_o \\ z_o \end{bmatrix} \quad (1)$$

where  $\Omega(t) = \Omega_0 + g_A t + \frac{1}{2}b_A t^2$  is the rotational speed of the target,  $\Omega_0$  is the rotational initial speed (RIS) of the target,  $g_A$  is the rotational acceleration (RA),  $b_A$  is the rotational acceleration change coefficient (RACC),  $\phi$  is the initial phase of the target's rotation,  $(x_o, y_o, z_o)$  is the coordinate representation of the origin  $o$  of the target's local coordinate system in the radar coordinate system, and  $\mathbf{R}_{\text{init}}$  is the Euler rotation matrix, determined by the initial Euler angles  $\alpha$ ,  $\beta$ , and  $\gamma$ , and its expression is

$$\begin{aligned} \mathbf{R}_{\text{init}} &= \begin{bmatrix} \cos \alpha & -\sin \alpha & 0 \\ \sin \alpha & \cos \alpha & 0 \\ 0 & 0 & 1 \end{bmatrix} \begin{bmatrix} 1 & 0 & 0 \\ 0 & \cos \gamma & -\sin \gamma \\ 0 & \sin \gamma & \cos \gamma \end{bmatrix} \begin{bmatrix} \cos \beta & -\sin \beta & 0 \\ \sin \beta & \cos \beta & 0 \\ 0 & 0 & 1 \end{bmatrix} \\ &= \begin{bmatrix} a_{11} & a_{12} & a_{13} \\ a_{21} & a_{22} & a_{23} \\ a_{31} & a_{32} & a_{33} \end{bmatrix} \end{aligned} \quad (2)$$

where

$$\begin{cases} a_{11} = \cos \alpha \cos \beta - \sin \alpha \cos \gamma \sin \beta \\ a_{12} = -\cos \alpha \sin \beta - \sin \alpha \cos \gamma \cos \beta \\ a_{13} = \sin \alpha \sin \gamma \\ a_{21} = \sin \alpha \cos \beta + \cos \alpha \cos \gamma \sin \beta \\ a_{22} = -\sin \alpha \sin \beta + \cos \alpha \cos \gamma \cos \beta \\ a_{23} = -\cos \alpha \sin \gamma \\ a_{31} = \sin \gamma \sin \beta \\ a_{32} = \sin \gamma \cos \beta \\ a_{33} = \cos \gamma \end{cases} \quad (3)$$

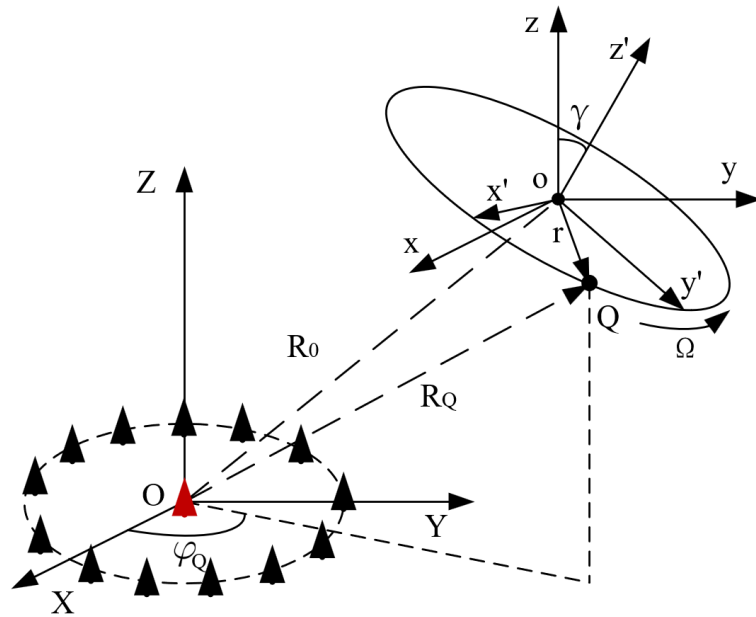


**Figure 1.** Variable-speed motion detection model under non-quasi-axial incidence conditions.

According to reference [10],  $\alpha$  and  $\beta$  are the rotation angles of the target around the  $Z$  axis, and the Doppler frequency shift curve is only affected by the initial phase by these two angles. Since the extraction of micro-motion parameters is independent of the initial phase of the target frequency shift curve, the rotation matrix  $\mathbf{R}_{\text{init}}$  can also be expressed as

$$\mathbf{R}_{\text{init}} = \begin{bmatrix} 1 & 0 & 0 \\ 0 & \cos \gamma & -\sin \gamma \\ 0 & \sin \gamma & \cos \gamma \end{bmatrix} \quad (4)$$

The target local coordinate system can be obtained by rotating the  $\gamma$  angle around the  $x$  axis of the reference coordinate system. Therefore, the target local coordinate system coincides with the  $X$  axis of the reference coordinate system. Therefore,  $o - xy'z'$  can be used to represent the target local coordinate system. Then, by combining Equations (1) and (4), the coordinates of target  $Q$  in the radar coordinate system can be obtained as

$$\begin{bmatrix} X_Q(t) \\ Y_Q(t) \\ Z_Q(t) \end{bmatrix} = \begin{bmatrix} r \cos(2\pi(\Omega_0 t + \frac{1}{2}g_A t^2 + \frac{1}{6}b_A t^3) + \phi) + x_o \\ r \sin(2\pi(\Omega_0 t + \frac{1}{2}g_A t^2 + \frac{1}{6}b_A t^3) + \phi) \cos \gamma + y_o \\ r \sin(2\pi(\Omega_0 t + \frac{1}{2}g_A t^2 + \frac{1}{6}b_A t^3) + \phi) \sin \gamma + z_o \end{bmatrix} \quad (5)$$

where  $\gamma$  is the angle between the  $oz'$  axis and the  $oz$  axis. The distance  $R_Q(t)$  between the target  $Q$  and the receiving antenna and the azimuthal angle  $\varphi_Q(t)$  of the target  $Q$  satisfy

$$\begin{cases} R_Q(t) = \sqrt{X_Q(t)^2 + Y_Q(t)^2 + Z_Q(t)^2} \\ \varphi_Q(t) = \arctan(Y_Q(t)/X_Q(t)) \end{cases} \quad (6)$$

At present, conventional techniques for generating vortex electromagnetic waves include the spiral shaping method, the circular array method, the traveling wave antenna method, and so on. As shown in Figure 1, this article adopts a single-transmitter multi-receiver vortex electromagnetic wave generation model, which uses a single antenna located at the coordinate origin as the transmitting antenna, emits a linear frequency modulation signal  $s(t) = \text{rect}(t/T_p) \exp(i2\pi(f_c t + 1/2Kt^2))$ , and has  $N$  antenna elements uniformly arranged on a circular ring as the receiving antenna. The phase shift  $\exp(il(2\pi/N)(n - 1))$ ,  $n = 1, 2, \dots, N$  is sequentially added to each element echo to generate vortex echoes. So, the echo of the target  $Q$  received by UCA is

$$s(t, l) = i^l \sigma_Q N J_l(k(t - \tau_Q(t))a \sin \theta_Q(t)) \text{rect}((t - \tau_Q(t))/T_p) \exp(il\varphi_Q(t)) \cdot \exp(i2\pi(f_c(t - \tau_Q(t)) + 0.5K(t - \tau_Q(t))^2)) + n(t) \quad (7)$$

where  $l$  is the mode number of vortex electromagnetic waves,  $\sigma_Q$  is the scattering coefficient of  $Q$ ,  $N$  is the number of antenna elements,  $k(t) = 2\pi(f_c + Kt)/c$ ,  $\tau_Q(t) = 2R_Q(t)/c$ ,  $f_c$ , and  $K$  are the carrier frequency and tuning frequency of the transmitted signal,  $c$  is the speed of light,  $J_l$  is the first-class  $l$ -order Bessel function,  $a$  is the radius of the UCA,  $\theta_Q(t)$  is the pitch angle of  $Q$ ,  $T_p$  is the pulse duration, the  $\text{rect}$  function is a rectangular window function, and  $n(t)$  is Gaussian white noise with zero mean, i.e.,  $n(t) \sim N(0, \sigma_n^2)$ . Due to the target speed being much lower than the speed of light, it can be assumed that the target remains relatively stationary with the radar during a single pulse duration. From this, it can be defined that  $t_m$  is the pulse emission time (slow time), and fast time  $t_k$  is the intra-pulse time. Equation (7) can be rewritten as

$$s(t_k, t_m, l) = i^l \sigma_Q N J_l(k(t_k - \tau_Q(t_m))a \sin \theta_Q(t_m)) \text{rect}((t_k - \tau_Q(t_m))/T_p) \cdot \exp(i2\pi(f_c(t_k - \tau_Q(t_m)) + 0.5K(t_k - \tau_Q(t_m))^2)) \exp(il\varphi_Q(t_m)) + n(t_m) \quad (8)$$

Then, according to the references [25–27], it can be seen that after performing dechirp processing on the above signal and performing fast Fourier transform on the fast time  $t_k$  dimension, the above equation becomes

$$S(f, t_m, l) = i^l \sigma_Q N \exp(il\varphi_Q(t_m)) H(f + K\tau_Q(t_m)) \exp(-i2\pi f_c \tau_Q(t_m)) \cdot \exp(-i2\pi(f + 0.5K\tau_Q(t_m))\tau_Q(t_m)) + n(t_m) \quad (9)$$

where  $H(f + K\tau_Q(t_m)) = \text{FFT}\left\{J_l(k(t_k - \tau_Q(t_m))a \sin \theta_Q(t_m)) \text{rect}\left(\frac{t_k - \tau_Q(t_m)}{T_p}\right)\right\}$ ,  $\text{FFT}\{\cdot\}$  is the fast Fourier transform, and the properties of  $H(f + K\tau_Q(t_m))$  are similar to the sinc function. After removing the residual video phase (RVP) term and envelope oblique (EO) term, the total echo can be written as

$$S_r(f, t_m, l) = i^l \sigma_Q N \exp(il\varphi_Q(t_m)) \exp(-i2\pi f_c \tau_Q(t_m)) H(f + K\tau_Q(t_m)) + n(t_m) \quad (10)$$

From the above analysis, it can be easily concluded that the echo of a single element in UCA is

$$s(t - \tau_Q(t)) = \sigma_Q \text{rect}((t - \tau_Q(t))/T_p) \exp(i2\pi(f_c(t - \tau_Q(t)) + 1/2K(t - \tau_Q(t))^2)) + n(t) \quad (11)$$

After performing the processing of Equations (8)–(10) on the above equation, it can be concluded that

$$s_{\text{dist}}(t_m) = \sigma_Q T_p \text{sinc}(T_p(f_i + K\tau_Q(t_m))) \exp(-i2\pi f_c \tau_Q(t_m)) + n(t_m) \quad (12)$$

where  $f_i$  is the peak frequency of the range slow time profile.

### 3. Algorithm for Extracting Three-Dimensional Information of Variable-Speed Moving Targets

Upon analyzing Equation (12), it can be inferred from the change law of the sinc function that Equation (12) reaches its maximum value at  $f_i + K\tau_Q(t_m) = 0$ , i.e.,  $f_i = -K\tau_Q(t_m)$ . We substitute  $\tau_Q(t_m) = 2R_Q(t_m)/c$  into the above equation, which can be simplified to  $f_i = -2KR_Q(t_m)/c$ .  $f_i$  can be transformed into the radial distance of a point target. At this point, from a slow time perspective, the peak value of the distance profile shows a curve that varies with  $R_Q(t_m)$ , which also reflects the motion characteristics of the scattering points. Therefore, in linear frequency modulation pulse radar, not only can the Doppler effect of the target be analyzed from the phase term, thanks to the high range resolution of the linear frequency modulation pulse radar, but the Doppler effect of the target can also be analyzed from the slow time plane. In addition, the equation for the variation curve of the peak position of the target's one-dimensional distance profile can be obtained by combining Equations (5) and (6) as follows:

$$R_Q(t_m) \approx (z_o^2 + 2rz_o \sin(2\pi\Omega t_m + \phi) \sin \gamma)^{1/2} \quad (13)$$

From Equation (13), it can be seen that on the slow time plane, the peak position of the distance image of the rotating scattering point exhibits a cosine variation with slow time. And when  $\sin(2\pi\Omega t_m + \phi) = 0$ ,  $R(t_m)$  can be obtained as

$$z_o \approx R(t_2) \quad (14)$$

where  $t_2$  is the corresponding  $t_m$  when  $\sin(2\pi\Omega t_m + \phi) = 0$ . Then, according to Equation (10), it can be seen that the phase term of the processed total echo is  $-2\pi f_c \tau_Q(t_m) + l\varphi_Q(t_m)$ . By taking its derivative, the total Doppler frequency shift  $f_{DI}$  of the target can be obtained as

$$\begin{aligned} f_{DI} &= f_L + f_R \\ &= \frac{1}{2\pi} \left( \frac{d(-4\pi f_c R_Q(t_m)/c)}{dt_m} + \frac{d(l\varphi_Q(t_m))}{dt_m} \right) \\ &\approx \frac{-4\pi f_c \Omega(t_m) r \sin \gamma}{c} \cos(2\pi\Omega t_m + \phi) \\ &\quad + \frac{l\Omega(t_m) r (r \cos \gamma + x_o \cos(2\pi\Omega t_m + \phi) \cos \gamma + y_o \sin(2\pi\Omega t_m + \phi))}{(r \cos(2\pi\Omega t_m + \phi) + x_o)^2 + (r \sin(2\pi\Omega t_m + \phi) \cos \gamma + y_o)^2} \end{aligned} \quad (15)$$

where  $f_L$  is a linear Doppler frequency shift caused by changes in the distance along the radar line of sight (LOS), and  $f_R$  is the rotational Doppler frequency shift induced by azimuthal change. Then, the Doppler frequency shift  $f_{D-I}$  when emitting vortex electromagnetic waves with opposite modes is

$$f_{D-I} \approx \frac{-4\pi f_c \Omega(t_m) r \sin \gamma}{c} \cos(2\pi\Omega t_m + \phi) - \frac{l\Omega(t_m) r (r \cos \gamma + x_o \cos(2\pi\Omega t_m + \phi) \cos \gamma + y_o \sin(2\pi\Omega t_m + \phi))}{(r \cos(2\pi\Omega t_m + \phi) + x_o)^2 + (r \sin(2\pi\Omega t_m + \phi) \cos \gamma + y_o)^2} \quad (16)$$

By combining Equations (15) and (16), it can be concluded that

$$\begin{cases} f_L = (f_{DI} + f_{D-I})/2 \\ \quad = \frac{-4\pi f_c \Omega(t_m) r \sin \gamma}{c} \cos(2\pi\Omega t_m + \phi) \\ f_R = (f_{DI} - f_{D-I})/2 \\ \quad = \frac{l\Omega(t_m) r (r \cos \gamma + x_o \cos(2\pi\Omega t_m + \phi) \cos \gamma + y_o \sin(2\pi\Omega t_m + \phi))}{(r \cos(2\pi\Omega t_m + \phi) + x_o)^2 + (r \sin(2\pi\Omega t_m + \phi) \cos \gamma + y_o)^2} \end{cases} \quad (17)$$

From Equation (17), the variation curves of the target's  $f_L$  and  $f_R$  can be obtained as shown in Figure 2. Obviously,  $f_L$  varies periodically with time. According to the analysis of the first term in Equation (17), it can be seen that  $\frac{-4\pi f_c \Omega(t_m) r \sin \gamma}{c}$  will only affect the amplitude of  $f_L$ , and the abscissa of the extreme value of  $f_L$  is only affected by  $\cos(2\pi\Omega t_m + \phi)$ . So, the abscissa distribution of the extreme points of  $f_L$  is consistent with the abscissa distribution of the extreme points of  $\cos(2\pi\Omega t_m + \phi)$ . When  $f_L$  reaches its

extreme value, it corresponds to  $\cos(2\pi\Omega t_m + \phi) = 1$  or  $\cos(2\pi\Omega t_m + \phi) = -1$ , that is,  $2\pi\Omega t_m + \phi = 0 + 2k\pi$  or  $2\pi\Omega t_m + \phi = \pi + 2k\pi$ , where  $k = 1, 2, 3, \dots$ . And, it is also easy to obtain that when  $t_m$  is taken as the mid-point of the two neighboring extreme points,  $2\pi\Omega t_m + \phi = \frac{\pi}{2} + p\pi$ , where  $p = 1, 2, 3, \dots$ .

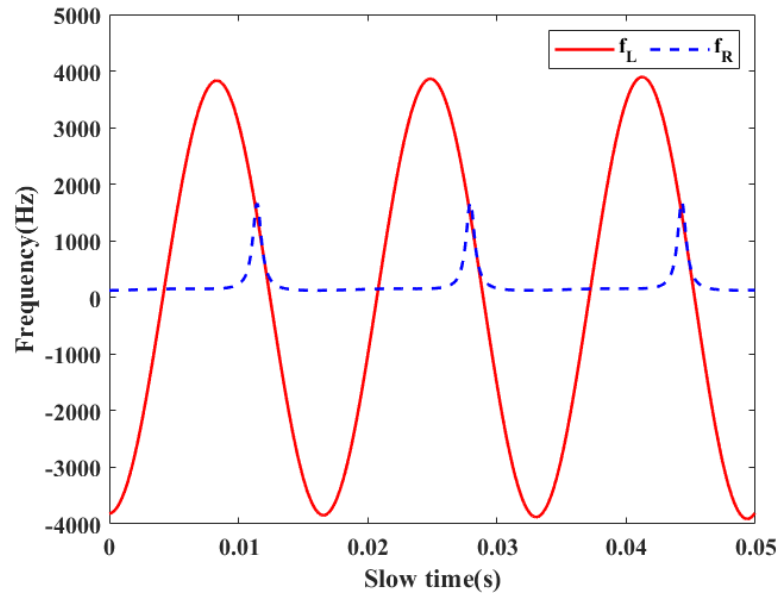


Figure 2. Frequency shift curves of  $f_L$  and  $f_R$ .

Then, we set the first and second extreme points of  $f_L$  as  $t_1$  and  $t_3$ . In addition, we set the median of the first and second extreme points of  $f_L$  as  $t_2$  and the median of the second and third extreme points as  $t_4$ . By observing the curve changes of  $f_L$ , we can locate the abscissa information corresponding to each extreme value and further obtain the median value corresponding to its adjacent abscissa. By using  $\cos(2\pi\Omega t_m + \phi)$ , the extreme and median information of the  $f_L$  can be transformed into the rotational speed change information of the target, i.e.,

$$\begin{cases} 2\pi(\Omega_0 t_1 + \frac{1}{2}g_A t_1^2 + \frac{1}{6}b_A t_1^3) + \phi = \pi \\ 2\pi(\Omega_0 t_2 + \frac{1}{2}g_A t_2^2 + \frac{1}{6}b_A t_2^3) + \phi = 3\pi/2 \\ 2\pi(\Omega_0 t_3 + \frac{1}{2}g_A t_3^2 + \frac{1}{6}b_A t_3^3) + \phi = 2\pi \\ 2\pi(\Omega_0 t_4 + \frac{1}{2}g_A t_4^2 + \frac{1}{6}b_A t_4^3) + \phi = 5\pi/2 \end{cases} \quad (18)$$

Then, simplifying the above equation gives

$$\begin{cases} \hat{b}_{A1} = ((\frac{3/4}{t_4-t_1} - \frac{1/4}{t_2-t_1})\frac{1}{t_4-t_2} - (\frac{2/4}{t_3-t_1} - \frac{1/4}{t_2-t_1})\frac{1}{t_3-t_2})\frac{6}{t_4-t_3} \\ \hat{g}_{A1} = ((\frac{3/4}{t_4-t_1} - \frac{1/4}{t_2-t_1})\frac{1}{(t_4-t_2)(t_4+t_2+t_1)} - (\frac{2/4}{t_3-t_1} - \frac{1/4}{t_2-t_1})\frac{1}{(t_3-t_2)(t_3+t_2+t_1)}) \\ \cdot \frac{2(t_4+t_2+t_1)(t_3+t_2+t_1)}{t_3-t_4} \\ \hat{\Omega}_{01} = (\frac{1}{4} - \frac{1}{6}\hat{b}_{A1}(t_2^3 - t_1^3) - \frac{1}{2}\hat{g}_{A1}(t_2^2 - t_1^2))/(t_2 - t_1) \\ \hat{\phi} = 2\pi - 2\pi(\hat{\Omega}_{01} t_3 + \frac{1}{2}\hat{g}_{A1} t_3^2 + \frac{1}{6}\hat{b}_{A1} t_3^3) \end{cases} \quad (19)$$

Due to the need for more time points to solve  $b_A$  and  $g_A$  and the accumulation of errors in extracting time points in the calculation, this leads to a relatively large error in  $b_A$  and  $g_A$ . However, according to the third term of Equation (19), it can be seen that in the process of solving  $\Omega_0$ , what is subtracted is  $b_A$  multiplied by the third power of time and  $g_A$  multiplied by the second power of time. Due to the relatively small values of  $b_A$  and  $g_A$  compared to  $\Omega_0$ , they will become smaller when multiplied by the power of time, thus weakening the impact of the estimation errors of  $b_A$  and  $g_A$  on solving  $\Omega_0$ . Therefore, in actual simulation,

the estimation error of  $\Omega_0$  is still relatively small. Furthermore, by substituting the first, third, and fifth extreme points in the frequency shift curve of  $f_L$  into  $f_R$ , we can obtain

$$\begin{cases} f_{R1} = \frac{I\Omega(t_1)r(r \cos \gamma - x_0 \cos \gamma)}{(-r+x_0)^2+y_0^2} \\ f_{R5} = \frac{I\Omega(t_5)r(r \cos \gamma - x_0 \cos \gamma)}{(-r+x_0)^2+y_0^2} \\ f_{R9} = \frac{I\Omega(t_9)r(r \cos \gamma - x_0 \cos \gamma)}{(-r+x_0)^2+y_0^2} \end{cases} \quad (20)$$

where  $t_5$  and  $t_9$  represent the time corresponding to the third and fifth extreme points, respectively, while  $f_{R1}$ ,  $f_{R5}$ , and  $f_{R9}$  represent the frequency values obtained by substituting the  $t_1$ ,  $t_5$ , and  $t_9$  into  $f_R$ . Then, using the above equation, we can obtain

$$\begin{cases} A = \frac{1}{l} \left( \frac{f_{R5}-f_{R1}}{t_5-t_1} - \frac{f_{R9}-f_{R1}}{t_9-t_1} \right) \frac{2}{t_5-t_9} = \frac{b_A r (r \cos \gamma - x_0 \cos \gamma)}{(-r+x_0)^2+y_0^2} \\ B = \frac{1}{l} \left( \frac{f_{R5}-f_{R1}}{t_5^2-t_1^2} - \frac{f_{R9}-f_{R1}}{t_9^2-t_1^2} \right) \frac{(t_5+t_1)(t_9+t_1)}{t_9-t_5} = \frac{g_A r (r \cos \gamma - x_0 \cos \gamma)}{(-r+x_0)^2+y_0^2} \\ C = \frac{1}{l} \left( \left( \frac{f_{R5}}{t_5} - \frac{f_{R1}}{t_1} \right) \frac{1}{t_5-t_1} - \left( \frac{f_{R9}}{t_9} - \frac{f_{R1}}{t_1} \right) \frac{1}{t_9-t_1} \right) \frac{t_1 t_5 t_9}{t_5-t_9} = \frac{\Omega_0 r (r \cos \gamma - x_0 \cos \gamma)}{(-r+x_0)^2+y_0^2} \end{cases} \quad (21)$$

where  $A$ ,  $B$ , and  $C$  respectively represent the right half of the first equal sign of the three sub-equations in Equation (21). Then, by further simplifying the above equation, it can be concluded that

$$\begin{cases} b_{A2} = \frac{A}{C} \hat{\Omega}_{01} \\ g_{A2} = \frac{B}{C} \hat{\Omega}_{01} \end{cases} \quad (22)$$

At this point, we can use the above equation and  $\hat{\Omega}_{01}$  to obtain new  $\hat{b}_A$  and  $\hat{g}_A$ , and we set them as  $b_{A2}$  and  $g_{A2}$ , respectively. Upon comparing Equations (19) and (21), it can be concluded that Equation (21) relies on fewer time points, so the error caused by extracting time points has a smaller impact on Equation (21). Therefore, the errors of  $b_{A2}$  and  $g_{A2}$  are smaller than those of  $b_{A1}$  and  $g_{A1}$ . Furthermore, when substituting  $t_1$  into  $f_L$ , it can be concluded that

$$f_{L1} \approx \frac{4\pi f_c \Omega(t_1) r \sin \gamma}{c} \quad (23)$$

where  $f_{L1}$  represents the frequency value obtained by substituting  $t_1$  into  $f_L$ . In addition, by substituting  $t_1$ ,  $t_2$ ,  $t_3$ , and  $t_4$  into  $f_R$  separately, we can obtain

$$\begin{cases} f_{R1} = \frac{I\Omega(t_1)r(r \cos \gamma - x_0 \cos \gamma)}{(-r+x_0)^2+y_0^2} \\ f_{R2} = \frac{I\Omega(t_2)r(r \cos \gamma - y_0)}{x_0^2+(-r \cos \gamma + y_0)^2} \\ f_{R3} = \frac{I\Omega(t_3)r(r \cos \gamma + x_0 \cos \gamma)}{(r+x_0)^2+y_0^2} \\ f_{R4} = \frac{I\Omega(t_4)r(r \cos \gamma + y_0)}{x_0^2+(r \cos \gamma + y_0)^2} \end{cases} \quad (24)$$

where  $f_{R2}$  and  $f_{R4}$  respectively represent the frequency values obtained by substituting  $t_2$  and  $t_4$  into  $f_R$ . Then, we substitute  $b_{A2}$ ,  $g_{A2}$ , and  $\hat{\Omega}_{01}$  into Equations (23) and (24), respectively, and then use the Trust Region Dogleg algorithm to solve the non-linear equation system composed of Equations (23) and (24), which can obtain the values of  $r$ ,  $\gamma$ ,  $x_0$ , and  $y_0$ . In summary, the process of parameter extraction for variable acceleration motion targets is shown in Figure 3, and the steps can be described as follows:

Step (1): A single array element receives the echo and performs dechirp processing, fast time domain  $t_k$  FFT, and then removes the RVP and EO terms to obtain the distance slow time map of the target. Then, the target position change is analyzed to extract the  $z_0$  coordinate of the target's rotation center.

Step (2): We synthesize the total vortex electromagnetic wave echo and perform the processing flow as shown in Equations (8)–(10). Then, we use the echo characteristics of two vortex electromagnetic waves with opposite modes to separate the linear and angular Doppler frequency shifts and extract the extremum and median information of  $f_L$ .

Step (3): We substitute the  $t_1, t_2, t_3,$  and  $t_4$  extracted in step (2) into Equation (19) to extract the initial values  $\hat{\phi}, \hat{\Omega}_{01}, \hat{b}_{A1},$  and  $\hat{g}_{A1}$  of  $\phi, \text{RIS}, \text{RA},$  and  $\text{RACC}$ .

Step (4): We substitute the  $t_1, t_3,$  and  $t_5$  extracted in step (2) into  $f_R$  to calculate  $A/C$  and  $B/C$ . Then, combined with the  $\hat{\Omega}_{01}$  obtained in step (3), we use Equation (22) to solve  $\hat{b}_{A2}$  and  $\hat{g}_{A2}$ .

Step (5): We substitute the  $t_1, t_2, t_3,$  and  $t_4$  extracted in step (2) into equations  $f_L$  and  $f_R$  to form a non-linear equation system. Then, we substitute the  $\hat{\Omega}_{01}$  obtained in step (3) and the  $\hat{b}_{A2}$  and  $\hat{g}_{A2}$  obtained in step (4) into the above equation system, and we use the Trust Region Dogleg algorithm to solve  $r, \gamma, x_o,$  and  $y_o$ .

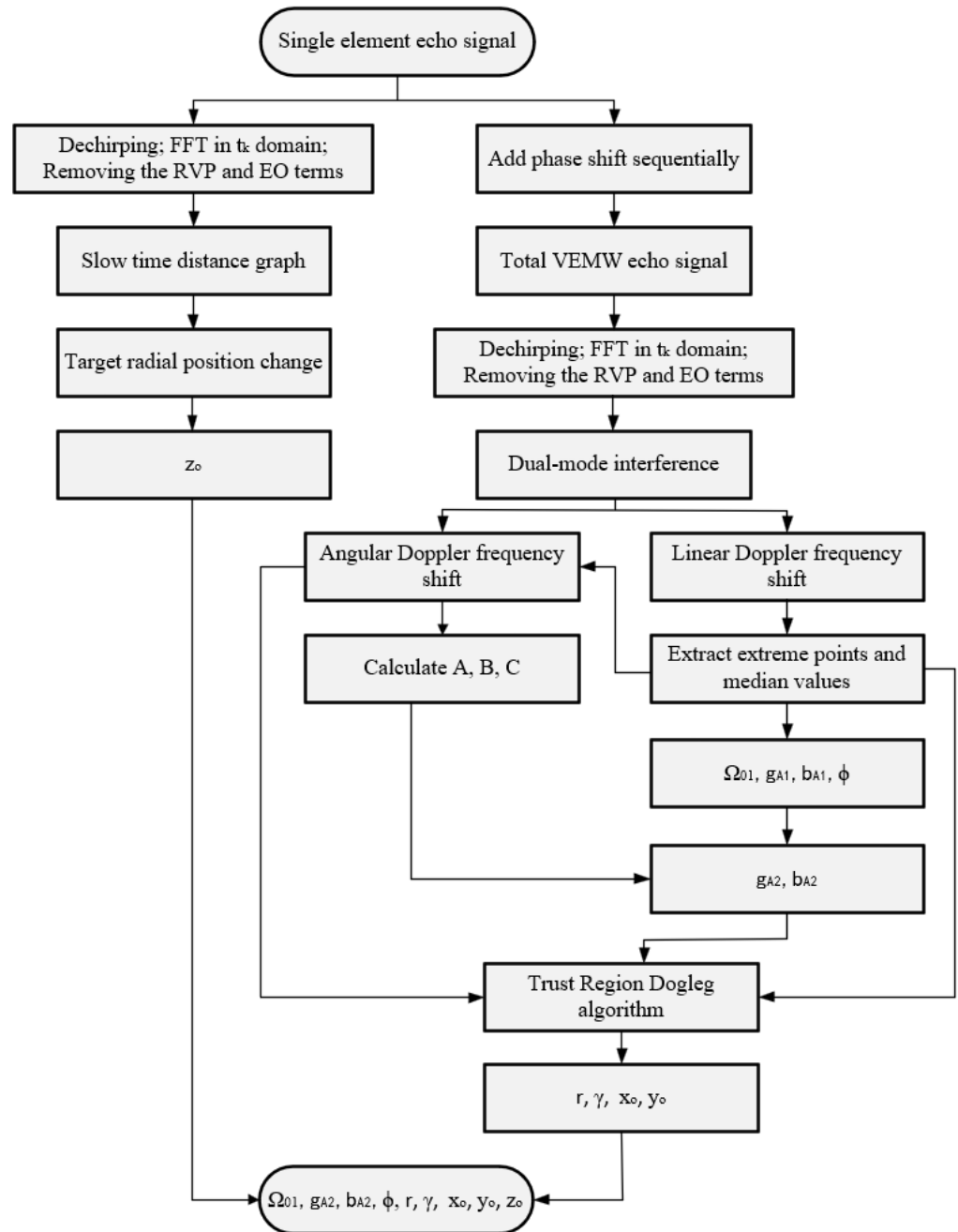


Figure 3. The flow chart for extracting three-dimensional parameters of variable-speed motion targets.

#### 4. Simulation Experiments and Result Analysis

In order to demonstrate the accuracy of the analysis and the effectiveness of the proposed parameter estimation method, corresponding simulation experiments were designed for verification, and the experimental results were analyzed. The specific experimental parameter settings are shown in Table 1.

**Table 1.** Main parameter settings in simulation.

Parameter	Value	Unit
Carrier frequency $f_c$	10	GHz
OAM mode $l$	4	\
Rotation radius $r$	0.3	m
Tilt angle $\gamma$	$\pi/6$	rad
RACC $b_A$	$50\pi$	rad/s <sup>2</sup>
RA $g_A$	$60\pi$	rad/s <sup>2</sup>
RIS $\Omega_0$	$120\pi$	rad/s
$(x_0, y_0, z_0)$	(0.1, 0.2, 29)	m

The theoretical and simplified change curves of the target's  $R_Q(t_m)$  can be obtained from Equations (5), (6) and (12), as shown in Figure 4. As shown in the figure, the theoretical curve and approximate curve basically overlap, and the impact of the approximate processing on the estimation of the distance between the target and the radar can be ignored. Then, based on the parameters set in Table 1, the slow time profile of the target can be obtained as shown in Figure 5. Comparing Figures 4 and 5, it can be observed that the radial motion changes of the target can be clearly observed from the distance slow time, and the target's  $z_0$  information can be extracted based on this. In addition, according to the parameters set in Table 1, the Choi–Williams distribution time–frequency analysis of the echoes was performed, and the target linear and angular Doppler shift curves were obtained as shown in Figures 6 and 7, respectively. According to the analysis in Section 3, the extreme points of  $f_L$  can be set as  $t_1, t_3, t_5$ , etc. in sequence while simultaneously setting the median values of two adjacent extreme points as  $t_2, t_4, t_6$ , etc. By extracting the first extreme value information in Figure 5 and combining it with the analysis in Equation (14), it can be concluded that  $z_0 = 28.968$  m. At this point, the estimation error of  $z_0$  was 0.11%. This indicates that the algorithm proposed in this article can effectively estimate the  $z_0$  coordinate of the rotation center.

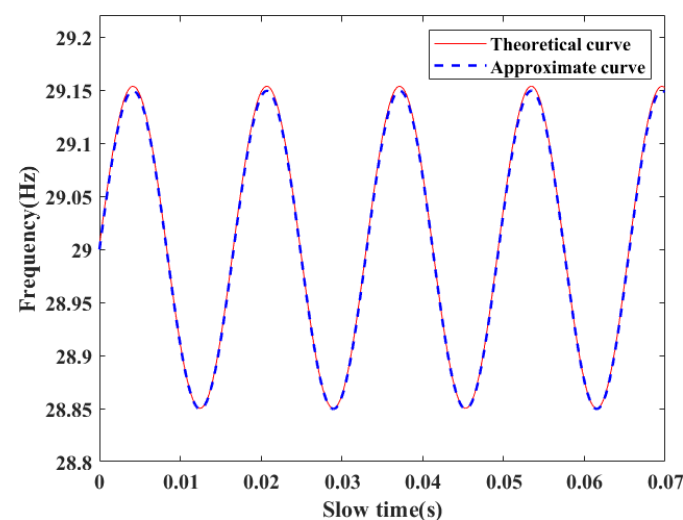


**Figure 4.** Theoretical and approximate curves of  $R_Q(t_m)$ .

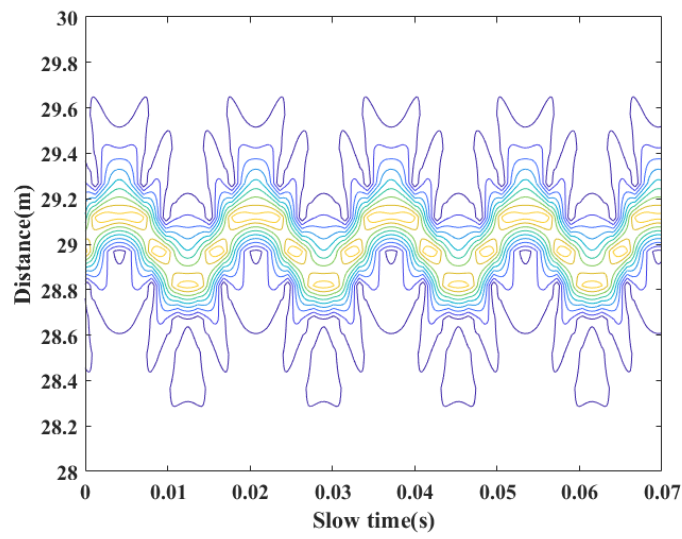


Figure 5. Target's distance slow time graph.

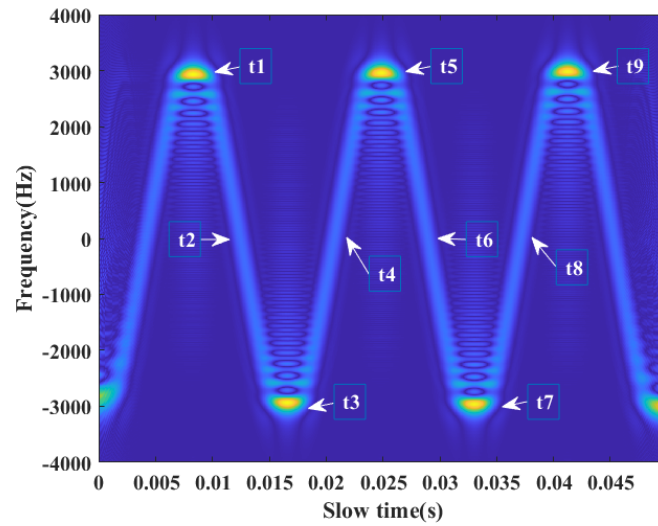


Figure 6. Linear Doppler shift curve of the target.

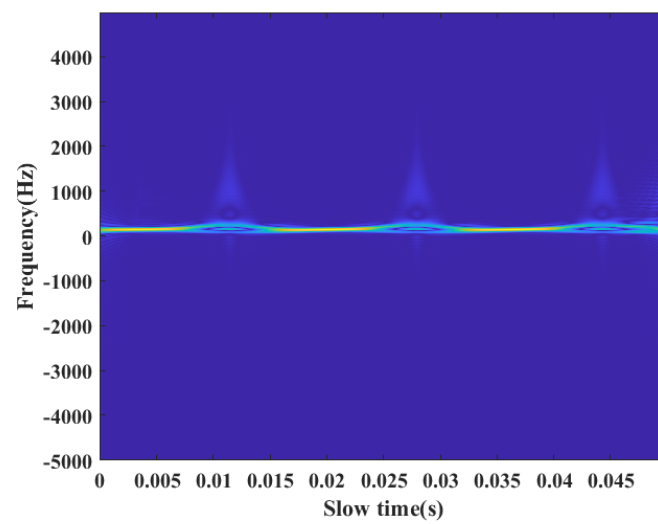


Figure 7. Angular Doppler shift curve of the target.

Then, by substituting the  $t_1, t_2, t_3$ , and  $t_4$  extracted from the above steps into Equation (19), the estimated value of RIS could be obtained as  $119.573 \pi\text{rad/s}$ . At this point, the estimated error of RIS was 0.4%. Furthermore, substituting  $t_1, t_5$ , and  $t_9$  into Equation (21) yielded  $A/C$  and  $B/C$  as 0.415 and 0.500, respectively. Then, by using Equation (22), it could be concluded that the estimated values of RA and RACC were  $59.810 \pi\text{rad/s}^2$  and  $49.641 \pi\text{rad/s}^2$ , respectively, with estimation errors of 0.3% and 0.7%. Then, the above estimated values were substituted into Equations (23) and (24), respectively, and the Trust Region Dogleg algorithm was used to solve the above equation system. And, it could be concluded that the estimated values of  $r, \gamma, x_o$ , and  $y_o$  were 0.304 m, 0.524 rad, 0.100 m, and 0.202 m, respectively. It could be calculated that the maximum relative error of the above parameters was less than 3.2%, which verifies the effectiveness of the proposed algorithm.

Furthermore, to study the performance of the algorithm under different motion states of objects, we designed three comparative experiments to study the relative errors of the algorithm under different  $b_A, g_A$ , and  $\Omega_0$  values. By changing the values of RIS, RA, and RACC separately, the variation of the  $f_L$  curve could be obtained, as shown in Figure 8. From the graph, it can be seen that the variation in the RIS had the greatest impact on the variation of the  $f_L$  curve, while the variation in the RA and RACC had a relatively small impact on the extreme value distribution of  $f_L$ , which may affect the extraction accuracy of the RA and RACC. Then, based on the parameter extraction process in Section 3, by changing the parameter range of the RA, the extraction errors of the other parameters could be obtained, as shown in Figure 9. As shown in the figure, when the RIS was varied within the range of  $[30 \pi\text{rad/s}, 319 \pi\text{rad/s}]$ , the extraction errors of each parameter were all less than 5%, which further proves the effectiveness of the algorithm proposed in this article. In addition, when the RIS was too low, the detection error increased significantly. This is because at this point, the influence of RIS on the distribution of extreme points on the  $f_L$  curve weakens, thus leading to a more sensitive perception of the change in extraction error of  $t$  during parameter solving and further leading to an increase in errors in various parameters. At the same time, when the RIS was too high, the detection accuracy of the algorithm also began to decrease. This is because the RIS is much larger than the RA and RACC at this time, thus resulting in a significant decrease in the values of  $A/C$  and  $B/C$  and causing smaller time extraction errors to have a significant impact on the  $A/C$  and  $B/C$  values, which ultimately leads to an increase in the RA and RACC extraction errors.

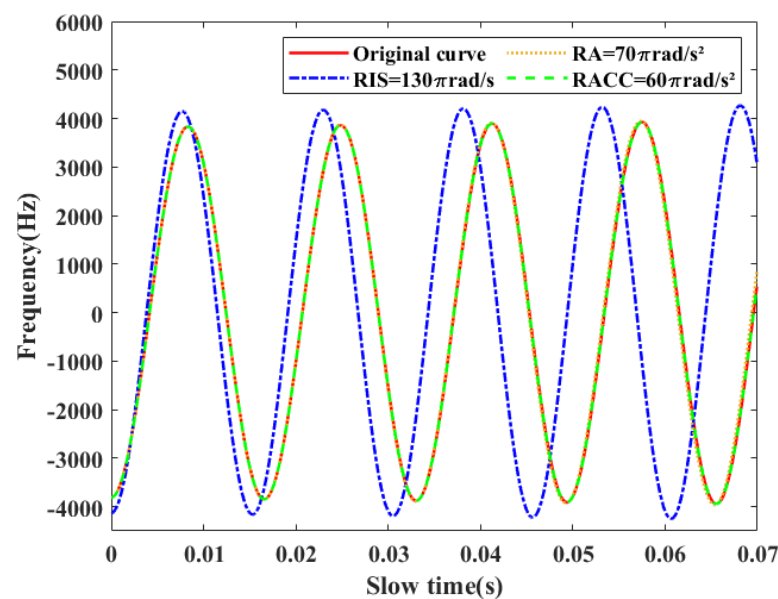
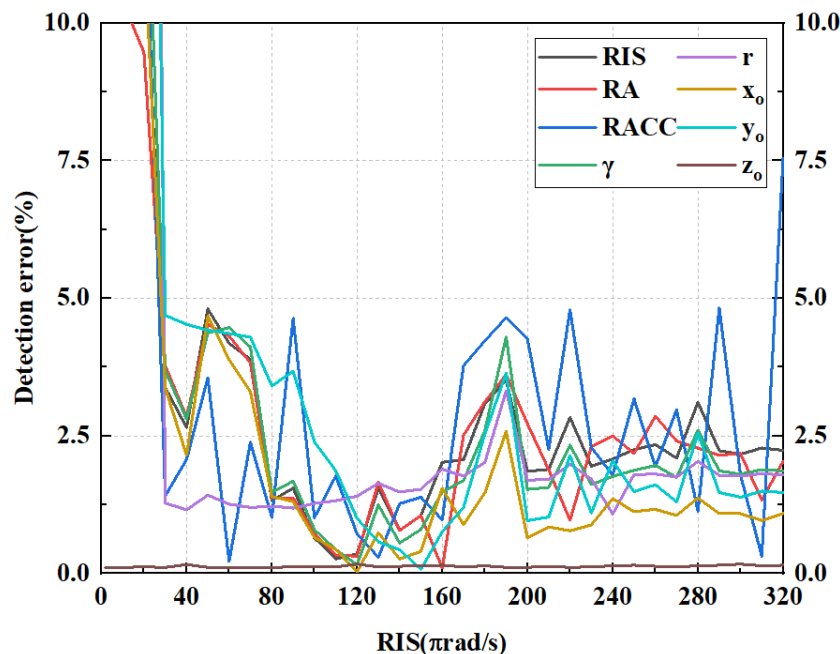


Figure 8. Linear Doppler frequency shift curves under different RIS, RA, and RACC conditions.



**Figure 9.** Error curves for parameter extraction under different RIS conditions.

Then, by changing the target's RA and RACC separately, the algorithm's parameter extraction error curves could be obtained, as shown in Figures 10 and 11. From the graph, it can be seen that under the condition of an error less than 5%, the acceleration range that the algorithm proposed in this paper could detect was  $[0.1 \pi\text{rad/s}^2, 124 \pi\text{rad/s}^2]$ , which means that accurate parameter extraction can also be achieved for variable-speed moving targets with small accelerations in this paper. Furthermore, by analyzing Figures 10 and 11, it can be concluded that the error curve of the rotation radius  $r$  was always relatively stable and has a smaller value, while the error of the rotation center  $y_o$  coordinate was relatively large. According to the analysis of Equations (23) and (24), it can be concluded that this is because the coupling between  $r$  and the equations is relatively high, while the coupling between  $y_o$  is relatively low. In addition, from Figures 9 and 10, it can be seen that the parameter extraction error of the RACC showed a relatively unstable trend compared to other parameters. This is because in the parameter settings of Figures 9 and 10, the ratio of the RACC to RIS was relatively small, so it was also sensitive to small time extraction errors, which caused the curve to shake. As the RACC increased, as shown in Figure 11, its trend gradually coincided with the RIS. Meanwhile, as shown in Figure 11, the range of the RACC that could be extracted in this article was  $[7 \pi\text{rad/s}^2, 4920 \pi\text{rad/s}^2]$ , which is far superior to existing algorithms. Furthermore, as shown in Figures 10 and 11, the overall trend of error was continuously increasing with the growth of the RA and RACC. From Equation (19), it can be seen that the parameter estimation accuracy of the algorithm in this paper is related to the extraction accuracy of time  $t_i$ . In this article, we extracted  $t_i$  based on the change curve of  $f_L$ . According to the simulation results, it can be seen that the distance between the different  $t_i$  values extracted by the above method was relatively small. It could be approximated that the change in  $A_{f_L}$  between  $t_1$  and  $t_2$  was small, that is, it could be regarded as a constant (where  $A_{f_L}$  is the amplitude of  $f_L$ ). Therefore, at this point, the change in  $f_L$  could be considered to be only related to  $\cos(2\pi\Omega t_m + \phi)$ , thus meaning that the extreme value of  $f_L$  is considered to be the same as the extreme value of  $\cos(2\pi\Omega t_m + \phi)$ . Based on this, we proposed Equation (18) and derived the extraction formulas for the RIS, RA, RACC, and  $\phi$ . However, when influenced by  $\Omega(t_m)$ ,  $A_{f_L}$  will vary over time. The accumulation becomes larger and larger, that is, it can no longer be regarded as a constant, but its impact on extreme value changes must be considered. Therefore, the error caused by the assumption that the extreme values of the two are the same will become larger over time, that is, as the value of  $A_{f_L}$  increases, it will become larger. As the

RA and RACC become larger,  $\Omega(t_m)$  will grow faster, and the time for  $A_{f_L}$  to be regarded as a constant will be shorter. This also explains why the error in Figures 10 and 11 increased with the increase in the RA and RACC values.

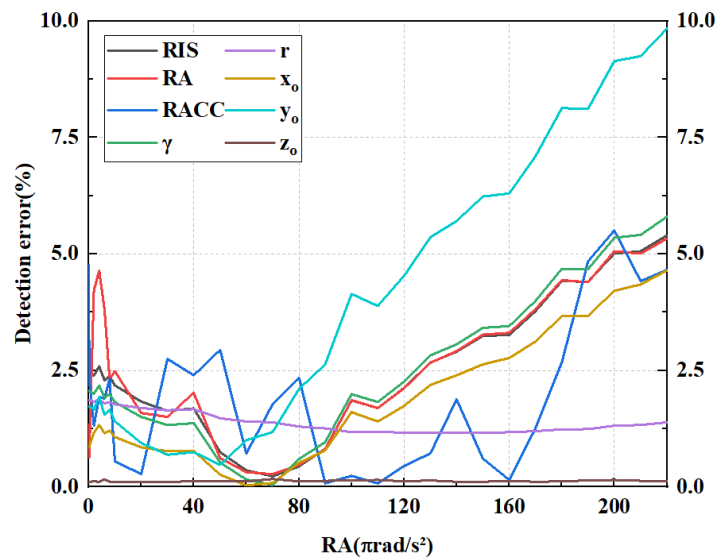


Figure 10. Parameter extraction under different RA conditions.

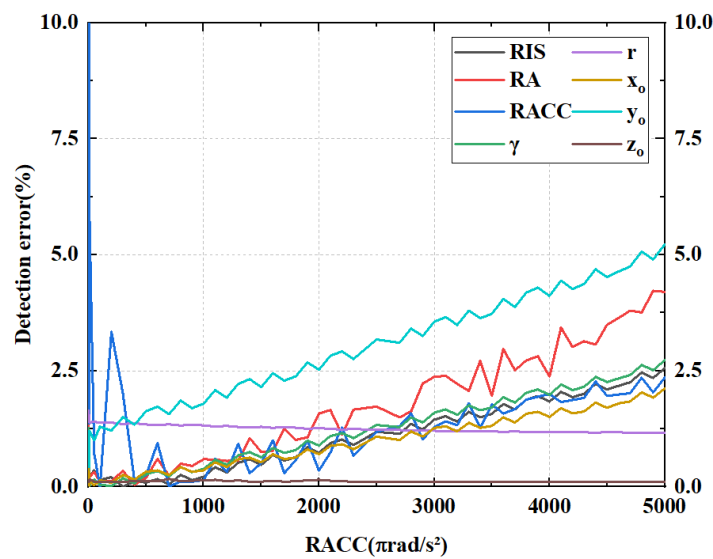


Figure 11. Parameter extraction under different RACC conditions.

However, in practical detection, there may still be situations where the target undergoes uniform acceleration motion. Based on this, this article set up an experiment with the RACC set to 0 to further consider the parameter extraction performance of the algorithm proposed in this article under uniform acceleration. The error curves for the parameter extraction are shown in Figures 12 and 13. Through simulation, it can be seen that the algorithm proposed in this article is suitable for extracting parameters of uniformly accelerating moving targets. Compared to the variable acceleration motion target, under the same parameter settings except for the RACC, this algorithm had smaller errors and a larger detectable range in the process of detecting uniformly accelerated motion targets. And, the range of detectable RIS and RA values under the condition of error less than 5% could be estimated as  $[50 \pi\text{rad/s}, 419 \pi\text{rad/s}]$  and  $[6 \pi\text{rad/s}^2, 278 \pi\text{rad/s}^2]$ , respectively.

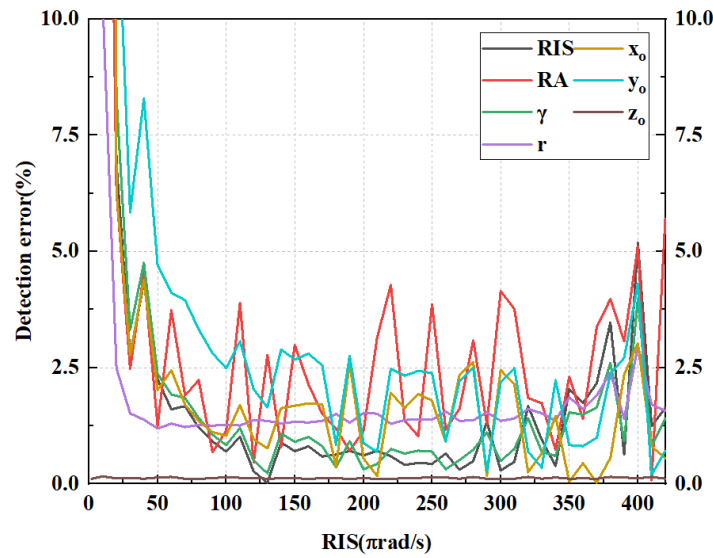


Figure 12. The error curve of parameter extraction under uniform acceleration conditions when RIS takes different values.

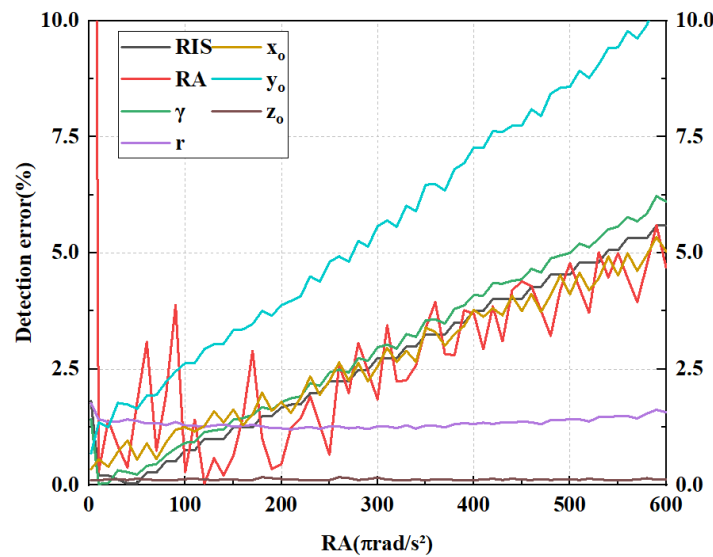


Figure 13. The error curve of parameter extraction under uniform acceleration conditions when RA takes different values.

Further considering that the initial phase of rotation also affects the distribution of extreme values and median values, we studied the extraction errors of various parameters under different initial phase conditions, and the results are shown in Figure 14. As shown in the figure, the values of the error curve at  $0, \pi,$  and  $2\pi$  were relatively large. From the analysis obtained in the above experiment, it can be seen that the error of the algorithm proposed in this article will increase over time. Due to the fact that this article determines the position of the extreme point by comparing the values on the left and right sides at a certain time point, in actual detection, the minimum  $t$  was 0. But when  $\phi = \pi,$   $f_L$  will reach its maximum value at  $t = 0,$  so the above method cannot extract the  $t$  corresponding to the first extreme value. Therefore, the first extracted time actually corresponds to the second extreme value. As the value of  $t_i$  increases, the values of the error curve at  $0, \pi,$  and  $2\pi$  will also increase. In addition, the variation curves for  $\phi = 0, 0.75\pi, \pi,$  and  $2\pi$  could be obtained from Equation (17), as shown in Figure 15. As shown in the figure, during the two changes of  $\phi$  from  $0$  to  $\pi$  and from  $\pi$  to  $2\pi,$   $t_i$  was continuously decreasing. Therefore, as shown in Figure 14, the error curves of the two ranges from  $0$  to  $\pi$  and from  $\pi$  to  $2\pi$  were

gradually decreasing. Furthermore, from the graph, it can be seen that under the condition of error less than 10%, the algorithm proposed in this article could achieve rotation phase extraction within the range of  $[9^\circ, 358^\circ]$ . To reduce the error corresponding to the initial phase of rotation mentioned above, we have further improved the method proposed in the article: as shown in Figure 14, except for  $\phi = 0^\circ, 180^\circ,$  and  $360^\circ$ , the value of the error variation curve of the initial phase of rotation was less than 5% and showed a decreasing trend in the range of  $0^\circ$  to  $180^\circ$  and  $180^\circ$  to  $360^\circ$ . Therefore, we set 5% as the comparison threshold. When the error value was higher than this value and increased compared to the previous position, we set the first time point as  $t_1$  and the one detected by the original algorithm as  $t_3$ . Based on the updated algorithm mentioned above, we remeasured the parameter extraction errors for  $\phi = 0^\circ, 180^\circ,$  and  $360^\circ$ , and the results are shown in Table 2.

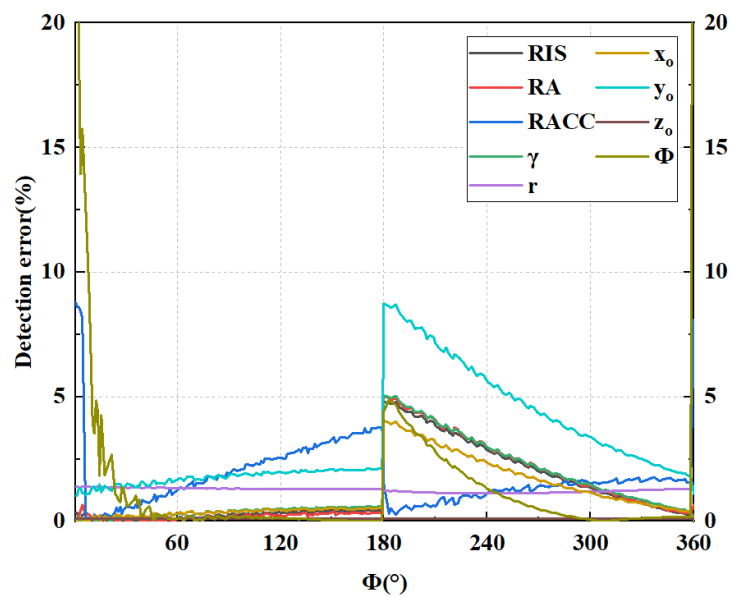


Figure 14. Parameter extraction under different  $\phi$  conditions.

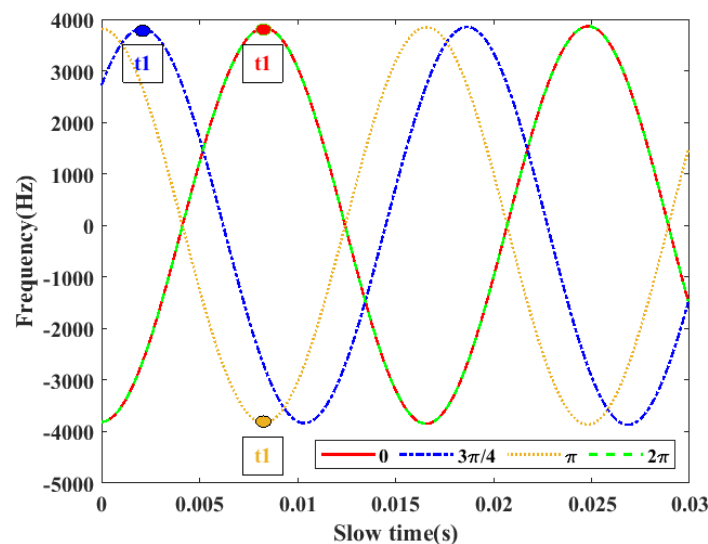
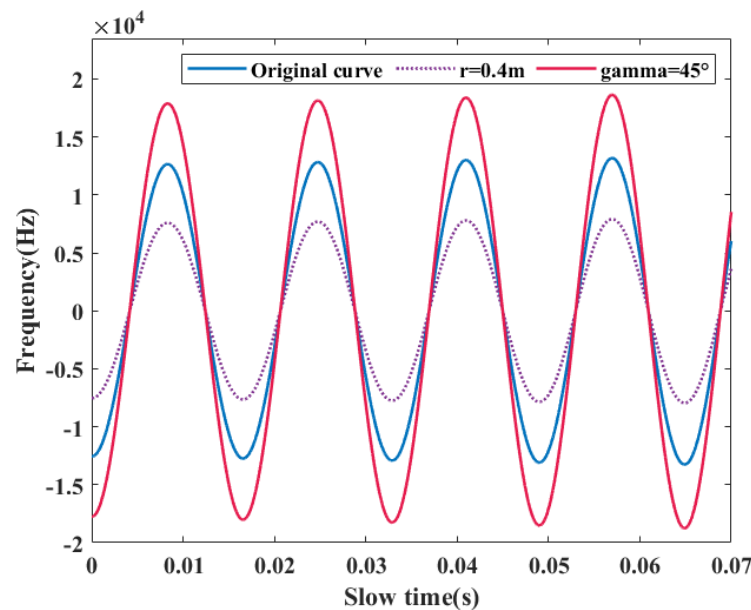


Figure 15. The variation curve of  $f_L$  at  $\phi = 0, 0.75\pi, \pi,$  and  $2\pi$ .

**Table 2.** Extraction errors of various parameters at  $\phi = 0^\circ, 180^\circ,$  and  $360^\circ$ .

Errors	RIS	RA	RACC	$\gamma$	$r$	$x_o$	$y_o$	$z_o$	$\phi$
$0^\circ$	0.23	1.55	2.84	0.29	1.23	0.83	1.68	0.10	0.43
$180^\circ$	0.40	0.23	2.34	0.59	1.33	0.09	2.04	0.11	0.05
$360^\circ$	0.23	1.55	2.84	0.29	1.23	0.83	1.68	0.10	0.43

In addition, according to Equations (17), (23) and (24), and the above analysis, it can be concluded that the rotation radius of the target and the inclination angle of non-quasi-axis incidence have a significant impact on the Doppler frequency shift variation and the accuracy of the Trust Region Dogleg algorithm. On this basis, we studied the performance of the algorithm under different rotation radii and tilt angles. The Doppler frequency shift changes after changing the  $r$  and  $\gamma$  are shown in Figure 16. The extraction error of each parameter is shown in Figures 17 and 18. Among them, the RIS, RA, RACC, and  $r$  were set to  $120 \pi \text{rad/s}$ ,  $100 \pi \text{rad/s}^2$ ,  $80 \pi \text{rad/s}^2$ , and  $0.4 \text{ m}$ , respectively. From Figures 9–11, it can be seen that the trend of  $x_o$  changes was roughly consistent with  $\Omega_0$ , while in Figures 17 and 18,  $x_o$  showed a completely different curve from  $\Omega_0$ . According to Equation (23), this is because  $x_o$  has strong coupling with  $r$  and  $\gamma$  in the system of equations. Therefore, when the sizes of  $r$  and  $\gamma$  change, the extraction error of  $x_o$  also changes accordingly. Furthermore, as shown in Figure 17, when  $r = 0.012 \text{ m}$ , the maximum parameter extraction error of the algorithm proposed in this article was 3.955%, which further proves that the algorithm can achieve accurate parameter extraction for smaller targets.

**Figure 16.** The variation curves of  $f_L$  under different  $r$  and  $\gamma$  conditions.

Furthermore, as shown in Figure 18, the error curve increased sharply when the tilt angle was less than  $10^\circ$ . This is because when the tilt angle is too small, the  $\cos \gamma$  approaches 1, which means that the detection model at this time is more similar to quasi-axis detection. Meanwhile, as shown in the figure, when the tilt angle approached  $60^\circ$ , the parameter error also increased. This is because at this point,  $\cos \gamma = y_o$  causes an equation in the non-linear system to become 0, thus making it unable to provide information for parameter estimation. At this point, substituting  $t_5$  into  $f_R$  can be used to supplement the information lost by the Trust Region Dogleg algorithm due to the equation being left and right to 0.

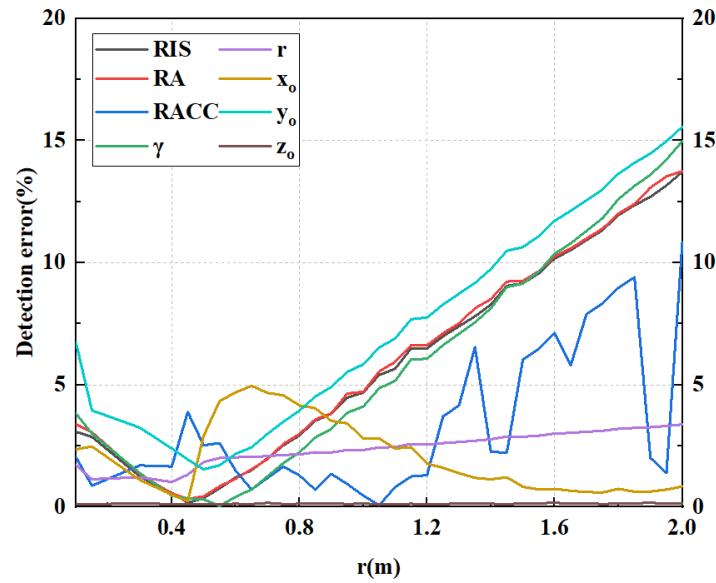


Figure 17. Error curves for parameter extraction under different  $r$  conditions.

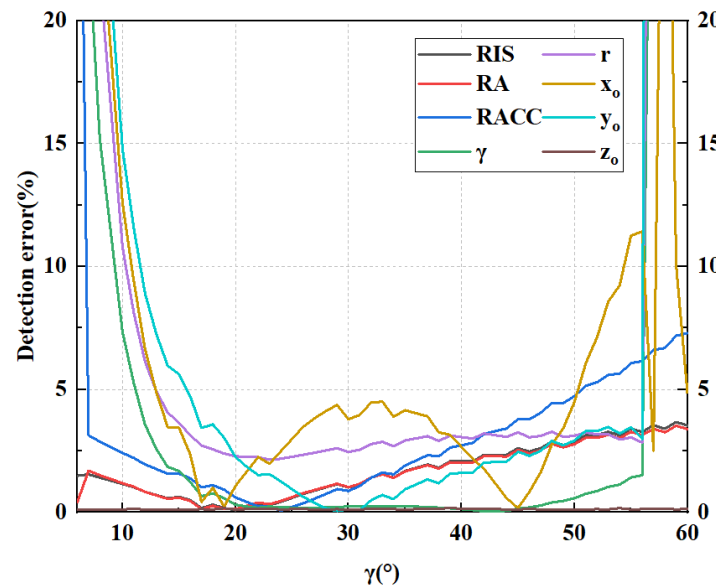


Figure 18. Error curves for parameter extraction under different  $\gamma$  conditions.

Additionally, to study the impact of noise interference on the algorithm proposed in this article, we designed six sets of experiments with SNRs of 5 dB, 10 dB, 15 dB, 20 dB, 25 dB, and 35 dB. And, the definition of the SNR is

$$R_{SN} = 10 \times \lg(\bar{P}_s/P_{Noise}) \tag{25}$$

where  $\bar{P}_s$  is the average signal power, and  $P_{Noise}$  is the noise power.

To avoid randomness, we conducted 100 Monte Carlo experiments under each SNR condition, with other parameter settings shown in Table 1. The parameter extraction errors for each group of experiments are shown in Figure 19. From the figure, it can be seen that the effect of noise interference on the acceleration parameter extraction is large, and it can be analyzed that this is because the noise will make the time–frequency curve jitter, which affects the distribution of the position of the extreme value point and further results in the decrease of the acceleration extraction accuracy. At the same time, because the RACC required the largest number of extreme points, it was most affected by noise. From the figure, it can be seen that when the SNR was 5 dB, except for the RACC estimation error of

9.4%, the estimation errors of other parameters were all less than 5.0%, which also verifies the robustness of the algorithm proposed in this article.

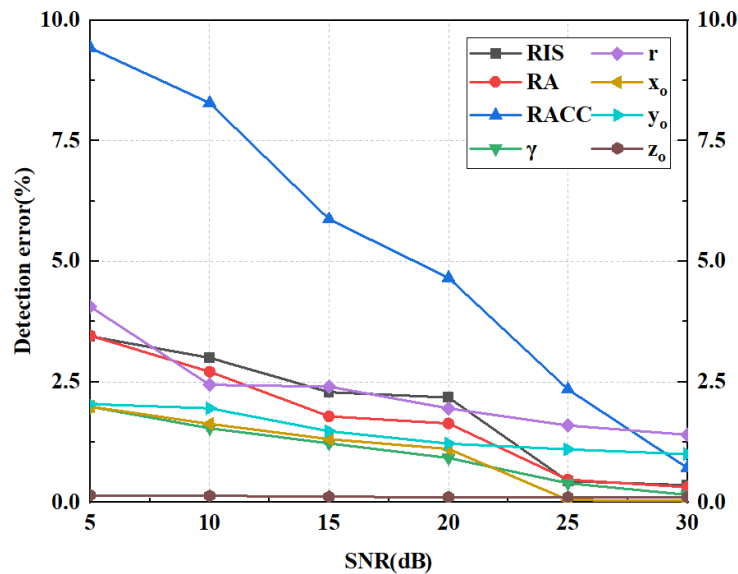


Figure 19. Error curves for parameter extraction under different SNR conditions.

Table 3 shows the performance comparison between the algorithm proposed in this paper and existing methods. The results show that, compared with the method proposed in [17], the algorithm proposed in this paper extends the application scenarios of the variable speed motion target parameter extraction algorithm from the quasi-axis to the non-quasi-axis. Compared to the method proposed in [19], our proposed method can extract more parameters from the target, but the accuracy was slightly lower than this method. Compared to the method proposed in [22], our characterization of the target structure was poor, but there was an improvement in system complexity.

Table 3. Performance comparison with existing methods.

Methods	Reference [17]	Reference [19]	Reference [21]	This Work
Target	VSMT	USMT	USMT	VSMT
Errors	RACC, RA, RIS, Initial phase < 6.3%	RIS, $r, \gamma < 0.2\%$	$\arctan\left(\frac{y_0}{x_0}\right) - \alpha, \beta, \gamma, \sqrt{x_0^2 + y_0^2}/r < 0.06\%$	RACC, RA, RIS, Initial phase, $x_0, y_0, z_0, r, \gamma < 1.5\%$
Incidence	Quasi-axis	Non-quasi-axis	Non-quasi-axis	Non-quasi-axis

Where USRT and VSRT represent the uniform motion targets and variable motion targets, respectively, with  $\alpha, \beta,$  and  $\gamma$  representing the three angles in the Euler matrix.

### 5. Conclusions

This article mainly studies the Doppler effect of variable-speed moving targets under non-quasi-axial incidence conditions of vortex electromagnetic waves and proposes a three-dimensional information extraction algorithm for variable-velocity moving targets based on single element echoes and all element echoes. Firstly, based on the single-element echo, the one-dimensional range profile of the target was extracted, and then the  $z_0$  coordinate of the target rotation center was extracted. Then, based on the synthesized vortex echo, the line and angle Doppler frequency shifts were separated, and the mathematical relationship between the extreme points and median values in the line Doppler frequency shift curve and the target's RA, RACC, and other parameters was further analyzed. Based on this, the acceleration and other information about the target were extracted. Then, the above extreme points, median values, etc. were substituted into  $f_L$  and  $f_R$  to form a non-linear

equation system. The Trust Region Dogleg algorithm was used to solve the equation, and the target rotation radius, rotation center  $x_o, y_o$  coordinates, and tilt angle were obtained. And, the performance of the algorithm was studied separately under different motion states, rotation radii, tilt angles, initial phases, and signal-to-noise ratios. Compared to existing acceleration extraction algorithms, this method can be applied to more complex application scenarios. In the future, the feasibility of the proposed method will be verified in practical scenarios, and further research will be conducted on scenarios where scattering points are indistinguishable.

**Author Contributions:** Conceptualization, L.Z. and Y.Z.; methodology, L.Z.; software, L.Z. and W.X.; formal analysis, L.Z. and Y.C.; data curation, L.Z. and H.Y.; writing—original draft preparation, L.Z.; writing—review and editing, L.Z., Y.C., and H.Y.; visualization, L.Z. and Y.C.; supervision, Y.Z.; project administration, Y.Z. and Y.C.; funding acquisition, Y.Z. and Y.C. All authors have read and agreed to the published version of the manuscript.

**Funding:** This work was supported by the National Natural Science Foundation of China under Grant 62371473, 61971434, as well as the Support Project for Youth Innovation Team of Shaanxi Universities.

**Data Availability Statement:** Due to the nature of this research, participants of this study did not agree for their data to be shared publicly, so supporting data is not available.

**Acknowledgments:** The authors would like to thank the handling editor and the anonymous reviewers for their valuable comments and suggestions for this article.

**Conflicts of Interest:** The authors declare no conflicts of interest.

## References

- Gao, S.; Ma, H.; Liu, H.; Yang, Y. DOD and DOA estimation from incomplete data based on PARAFAC and atomic norm minimization method. *IEEE Trans. Geosci. Remote Sens.* **2023**, *61*, 5100314. [\[CrossRef\]](#)
- Chen, Y.; Wang, S.; Luo, Y.; Liu, H. Measurement matrix optimization based on target prior information for radar imaging. *IEEE Sens. J.* **2023**, *23*, 9808–9819. [\[CrossRef\]](#)
- Zhang, H.; Ni, J.; Zhang, C.; Luo, Y.; Zhang, Q. PnP-Based ground moving target imaging network for squint SAR and sparse sampling. *IEEE Trans. Geosci. Remote Sens.* **2024**, *62*, 5201020. [\[CrossRef\]](#)
- Yang, Y.; Cheng, Y.; Wu, H.; Yang, Z.; Wang, H. Parametric Instantaneous Frequency Estimation via PWSR With Adaptive QFM Dictionary. *IEEE Signal Process. Lett.* **2023**, *30*, 738–742. [\[CrossRef\]](#)
- Tamburini, F.; Mari, E.; Sponselli, A.; Thidé, B.; Bianchini, A.; Romanato, F. Encoding many channels on the same frequency through radio vorticity: First experimental test. *New J. Phys.* **2012**, *14*, 033001. [\[CrossRef\]](#)
- Li, C.; Li, S.; Dong, Y.; Peng, W.; Li, J.; Li, Y.; Li, Q.; Chen, Z. Targets' Radial and Tangential Velocities Estimation Based on Vortex Electromagnetic Waves. *Remote Sens.* **2022**, *14*, 3861. [\[CrossRef\]](#)
- Mao, R.; Liu, K.; Liu, H.; Yang, Y.; Xiao, H. Electromagnetic vortex imaging based on OAM multiplexing beam with orthogonal polyphase coding. *IEEE Sens. J.* **2023**, *24*, 30786–30793. [\[CrossRef\]](#)
- Wang, Z.; Chen, Y.; Yuan, H.; Luo, Y.; Zhang, Q. Real Micro-Doppler Parameters Extraction of Spinning Targets Based on Rotating Interference Antenna. *Remote Sens.* **2022**, *14*, 5300. [\[CrossRef\]](#)
- Wang, J.; Liu, K.; Wang, Y.; Liu, H.; Cheng, Y.; Wang, H. A novel forward-Looking target reconstruction method with electromagnetic vortex interferometry. *IEEE Trans. Microw. Theory Tech.* **2023**, *71*, 5428–5444. [\[CrossRef\]](#)
- Yuan, H.; Zhao, S.; Chen, Y.; Luo, Y.; Liu, Y.; Zhang, Y. Micromotion Parameters Estimation of Precession Cone Based on Monostatic Radars. *IEEE Trans. Antennas Propag.* **2024**, *72*, 2811–2824. [\[CrossRef\]](#)
- Zhu, Y.; Zhou, Y.; Chen, Y.; Bu, L.; Zhao, H. A mode optimization method for vortex electromagnetic wave radar imaging. *IEEE Geosci. Remote Sens. Lett.* **2022**, *19*, 4024405. [\[CrossRef\]](#)
- Qiu, S.; Ding, Y.; Liu, T.; Liu, Z.L.; Ren, Y. Rotational object detection at noncoaxial light incidence based on the rotational Doppler effect. *Opt. Express* **2022**, *30*, 20441–20450. [\[CrossRef\]](#)
- Liang, J.; Chen, Y.; Zhang, Q.; Luo, Y.; Li, X. Three-Dimensional Imaging of Vortex Electromagnetic Wave Radar with Integer and Fractional Order OAM Modes. *Remote Sens.* **2023**, *15*, 2903. [\[CrossRef\]](#)
- Ma, H.; Liu, H. Waveform Diversity-Based Generation of Convergent Beam Carrying Orbital Angular Momentum. *IEEE Trans. Antennas Propag.* **2020**, *68*, 5487–5495. [\[CrossRef\]](#)
- Zhou, Z.; Cheng, Y.; Liu, K.; Liu, H. Detection of uniformly accelerated spinning target based on OAM beams. In Proceedings of the 2018 International Conference on Microwave and Millimeter Wave Technology (ICMMT), Chengdu, China, 7–11 May 2018; pp. 1–3.
- Wang, Y.; Wang, Y.; Guo, K.; Guo, Z. Detecting targets' longitudinal and angular accelerations based on vortex electromagnetic waves. *Measurement* **2022**, *187*, 110278. [\[CrossRef\]](#)

17. Zhang, L.; Zhu, Y.; Chen, Y.; Xie, W. Parameter extraction of accelerated motion targets based on vortex electromagnetic wave radar. *IEEE Geosci. Remote Sens. Lett.* **2023**, *20*, 3506505. [[CrossRef](#)]
18. Luo, Y.; Chen, Y.; Zhu, Y.; Li, W.; Zhang, Q. Doppler effect and micro-Doppler effect of vortex-electromagnetic-wave-based radar. *IET Radar Sonar Navig.* **2020**, *14*, 2–9. [[CrossRef](#)]
19. Wang, Y.; Liu, K.; Liu, H.; Wang, J.; Cheng, Y. Detection of rotational object in arbitrary position using vortex electromagnetic waves. *IEEE Sens. J.* **2021**, *21*, 4989–4994. [[CrossRef](#)]
20. Yuan, H.; Luo, Y.; Chen, Y.; Liang, J.; Liu, Y. Micro-motion parameter extraction of rotating target based on vortex electromagnetic wave radar. *IET Radar Sonar Navig.* **2021**, *15*, 1594–1606. [[CrossRef](#)]
21. Lv, K.; Ma, H.; Jiang, X.; Bai, J.; Liu, H. Micromotion Feature Extraction with VEMW Radar Based on Rotational Doppler Effect. *Remote Sens.* **2023**, *15*, 2847. [[CrossRef](#)]
22. Han, X.; Du, L.; Liu, H. Feature extraction of space cone-shaped target based on narrow-band radar networks. *J. Electron. Inf.* **2014**, *36*, 2956–2962.
23. Zhou, H.; Peng, C.; Guo, K.; Lei, Y.; Guo, Z. Estimating Parameters of Ballistic Target by Single Hybrid Radar Based on Vortex and Wideband Electromagnetic Waves. *IEEE Sens. J.* **2023**, *23*, 26423–26429. [[CrossRef](#)]
24. Zhang, J.; Xu, C. Trust region dogleg path algorithms for unconstrained minimization. *Ann. Oper. Res.* **1999**, *87*, 407–418. [[CrossRef](#)]
25. Bu, L.; Zhu, Y.; Chen, Y.; Song, X.; Yang, Y.; Zang, Y. Micro-motion parameter extraction of multi-scattering-point target based on vortex electromagnetic wave radar. *Remote Sens.* **2022**, *14*, 5908 [[CrossRef](#)]
26. Yuan, H.; Chen, Y.; Luo, Y.; Liang, J.; Wang, Z. A Resolution-Improved Imaging Algorithm Based on Uniform Circular Array. *IEEE Antennas Wirel. Propag. Lett.* **2022**, *21*, 461–465. [[CrossRef](#)]
27. Wang, J.; Liu, K.; Cheng, Y.; Wang, H. Three-Dimensional Target Imaging Based on Vortex Stripmap SAR. *IEEE Sens. J.* **2019**, *19*, 1338–1345. [[CrossRef](#)]

**Disclaimer/Publisher’s Note:** The statements, opinions and data contained in all publications are solely those of the individual author(s) and contributor(s) and not of MDPI and/or the editor(s). MDPI and/or the editor(s) disclaim responsibility for any injury to people or property resulting from any ideas, methods, instructions or products referred to in the content.